Letters

OPEN ACCESS

Letter

Energy efficiency of reactive species generation in radio frequency atmospheric pressure plasma jets driven by tailored voltage waveforms in a He/O$_2$ mixture

Máté Vass[1,2,*] , **David Schulenberg**[1] , **Zoltán Donkó**[2] , **Peter Hartmann**[2] ,
David Steuer[3] , **Marc Böke**[4] , **Volker Schulz-von der Gathen**[4] , **Ihor Korolov**[1] ,
Thomas Mussenbrock[1] **and Julian Schulze**[1]

[1] Chair of Applied Electrodynamics and Plasma Technology, Ruhr-University Bochum, 44780 Bochum, Germany
[2] Institute for Solid State Physics and Optics, HUN-REN Wigner Research Centre for Physics, 1121 Budapest, Hungary
[3] Plasma Interface Physics, Ruhr-University Bochum, 44801 Bochum, Germany
[4] Experimental Physics II: Physics of Reactive Plasmas, Ruhr-University Bochum, 44801 Bochum, Germany

E-mail: vass@aept.rub.de

CrossMark

Abstract

The effect of the shape of the applied voltage waveform on the energy efficiency of reactive species generation is investigated in an atmospheric pressure RF microplasma jet operated in a He/O$_2$ mixture (99.5%/0.5%) based on a one-dimensional hybrid fluid-kinetic simulation method. Using a tailored waveform synthesized from four consecutive harmonics (with a base frequency of $f_b = 13.56$ MHz and amplitudes of $(160/k)$ V for the k-th harmonic), it is shown that by changing the identical phases of the even harmonics in the waveform, φ, the generation efficiencies of three specific reactive species (helium metastables, atomic and vibrationally excited oxygen), defined as the ratio of mean density and input plasma power, attain their maxima for different values of φ, due to changes in the Electron Energy Probability Function (EEPF). The phase control of the EEPF and its critical role in modulating generation energy efficiencies are explained in detail. The simulation results are verified by experimental (Phase Resolved Optical Emission Spectroscopy and Two Photon Absorption Laser Induced Fluorescence) data.

* Author to whom any correspondence should be addressed.

Atmospheric pressure radio-frequency (RF-) microplasma jets (μAPPJs) have a wide range of industrial applications, most notably in plasma medicine [1, 2], due to the generation of reactive oxygen and nitrogen species (RONS) [3–5]. These plasmas have been extensively studied experimentally including the exploration of new designs [6–8] and diagnostic methods [9–11] as well as computationally, including 0d models [12, 13] fluid models [14, 15], hybrid models [16–18] and fully kinetic PIC/MCC models [19, 20]. It has been shown that using well-chosen multi-frequency excitation waveforms with fixed harmonics' phases (Voltage Waveform Tailoring) enables the energy efficient generation of specific radicals by tailoring the Electron Energy Probability Function (EEPF) [21–23]. This is based on the efficient transfer of power from the generator into the plasma, which is possible for tailored voltage waveforms based on the latest generation of multi-frequency impedance matchings [24, 25]. In this work we show, based on experimental as well as simulation results of the COST reference jet [6] operated in a He/O$_2$ mixture, that altering the identical phases of the even harmonics, φ, in an excitation waveform consisting of four consecutive harmonics affects the energy efficiency of generating various neutral species in different ways. The optimal phase for maximizing the generation efficiency is found to vary among different species.

The simulation results presented in this paper were obtained from a spatially one-dimensional hybrid fluid-Monte Carlo simulation method [16]: a fluid module, solving the continuity equation based on the drift-diffusion approximation, along with Poisson's equation, is augmented by a Monte Carlo (MC-) module, which generates spatio-temporally resolved electron impact rates based on cross sections and the electric field calculated in the fluid module. Additionally, the fluid module updates the densities of the neutral species using a time-slicing method [17]. The two modules (fluid and MC) are run in an iterative manner (after every ≈ 100 RF-cycles the electron impact rates are re-calculated) until convergence is achieved (typically after $\approx 2 \times 10^3$ simulated RF-cycles).

In the discharge model 7 charged species (electrons, He$^+$, O$_2^+$, O$^+$, O$^-$, O$_2^-$ and O$_3^-$ ions) and 8 neutral species (O, He*, O(^{1}D), O$_2(v = 1 - 4)$, O$_2(a^1\Delta_g)$, O$_2(b^1\Sigma_g)$, O$_3$, O$_3(v)$) are considered. Here He* denotes an 'aggregate' species of the He(2^1S) and He(2^3S) metastable atoms [26]. The plasma surface interaction is modelled by assuming electron reflection, secondary electron emission by positive ions and surface loss for neutral species. The input parameters for the model (mobility and diffusion coefficients, surface coefficients, chemical reaction set) are identical to that reported in [16]. The chemistry set can be found in [27]. The set of electron impact processes is shown in table 1. Note, that processes 2 and 3 in the table denote the sum of all triplet and singlet excitations of helium: we assume that 50% of these collisions result in the creation of metastables [26]. A neutral gas pressure of

$p = 10^5$ Pa, with a constant gas temperature of $T_g = 350$ K was used. The gas mixture was set to 99.5% He and 0.5% O$_2$.

A schematic of the jet is shown in figure 1. The simulation uses an equidistant mesh with $N_g = 800$ gridpoints to resolve the $L = 1$ mm distance between the electrodes. The number of time steps within one RF-cycle is taken to be $N_t = 15\,000$ in the fluid module, while in the MC-simulation it is 2.76×10^6 to ensure a collision probability below 5% within a time step.

The powered electrode (situated at $x = 0$) is driven by the following voltage waveform:

$$\phi(t) = \sum_{k=1}^{4} \phi_k \cos\left(2\pi k f_b t + \varphi_k\right), \tag{1}$$

where $\phi_k = (160, 120, 80, 40)$ V, $f_b = 13.56$ MHz, and $\varphi_k = (0, \varphi + \pi, 0, \varphi + \pi)$ with φ the phase parameter for the even harmonics. Figure 2(a) shows $\phi(t)$ over two RF-periods (T) for various phase values: by changing φ from 0 to π, the waveform transitions between the 'valleys' and 'peaks' types [31].

Figure 2(b) shows the total power input to the plasma, P, for various phases, obtained from experiments (for the detailed method see [21]) and calculated from simulations (as $V\sum_k\langle j_k E\rangle$, with V the volume of the jet (30 mm^3), E the electric field and j_k the conduction current density of the k-th charged species. The angular brackets denote a spatio-temporal average). The trends observed in the simulation and experimental values align perfectly; however, their absolute values differ. This discrepancy arises because the study employs only spatially one-dimensional simulations, which inherently overestimate the power. This approximation fails to capture, e.g., the density decrease near the walls. The total power shows a cosine-shaped dependence as a function of the phase: that is, the highest absolute power absorbed by the plasma is observed in the case of either the 'valleys' or the 'peaks' waveforms, which exhibit sharp peaks at distinct times (cf figure 2(a)). In order to show that different neutral species attain their highest generation efficiency at different values of φ in the excitation waveform given by equation (1), the following neutrals will be investigated in more detail in the following: atomic oxygen, O, vibrationally excited oxygen molecules, O$_2(v)$, and helium metastables, He* (cf table 1). These species serve as representative examples of species that are generated by electrons at low, intermediate, and high energies, i.e. based on different parts of the EEPF.

Figure 3 shows the spatially averaged densities of atomic oxygen (panel (a)), showing simulation and experimental data, the latter from TALIF measurements in the 'middle' of the jet, (cf figure 1; for details on the experimental setup and the measurement technique, see [10]), as well as simulation data for the densities of the other two neutral species, He* and O$_2(v)$ (b) as a function of the phase. Furthermore, panels (c) and (d) depict the species' generation efficiency against φ, defined as mean

Table 1. List of electron impact processes considered in the simulation.

#	Reaction	Process	ε_{thr}	References
1	$e^- + He \longrightarrow e^- + He$	Elastic scattering	—	[28]
2	$e^- + He \longrightarrow e^- + He^*$	Triplet excitation	19.82 eV	[28]
3	$e^- + He \longrightarrow e^- + He^*$	Singlet excitation	20.61 eV	[28]
4	$e^- + He \longrightarrow e^- + He^+ + e^-$	Ionization	24.59 eV	[28]
5	$e^- + O_2 \longrightarrow O_2 + e^-$	Elastic scattering	—	[28]
6	$e^- + O_2(r=0) \longrightarrow e^- + O_2(r>0)$	Rotational excitation	0.02 eV	[29]
7	$e^- + O_2(v=0) \longrightarrow e^- + O_2(v=1)$	Vibrational excitation	0.19 eV	[29]
8	$e^- + O_2(v=0) \longrightarrow e^- + O_2(v=2)$	Vibrational excitation	0.38 eV	[29]
9	$e^- + O_2(v=0) \longrightarrow e^- + O_2(v=3)$	Vibrational excitation	0.57 eV	[29]
10	$e^- + O_2(v=0) \longrightarrow e^- + O_2(v=4)$	Vibrational excitation	0.75 eV	[29]
11	$e^- + O_2 \longrightarrow e^- + O_2(a^1\Delta_g)$	Metastable excitation	0.98 eV	[29]
12	$e^- + O_2 \longrightarrow e^- + O_2(b^1\Sigma_g)$	Metastable excitation	1.63 eV	[29]
13	$e^- + O_2 \longrightarrow O + O^-$	Dissociative attachment	4.2 eV	[29]
14	$e^- + O_2 \longrightarrow e^- + O_2$	Excitation	4.5 eV	[29]
15	$e^- + O_2 \longrightarrow O + O + e^-$	Dissociation	6.0 eV	[29]
16	$e^- + O_2 \longrightarrow O + O(^1D) + e^-$	Dissociation	8.4 eV	[29]
17	$e^- + O_2 \longrightarrow O(^1D) + O(^1D) + e^-$	Dissociation	9.97 eV	[29]
18	$e^- + O_2 \longrightarrow O_2^+ + e^- + e^-$	Ionization	12.06 eV	[30]
19	$e^- + O_2 \longrightarrow e^- + O + O(3p^3p)$	Dissociative excitation	14.7 eV	[29]
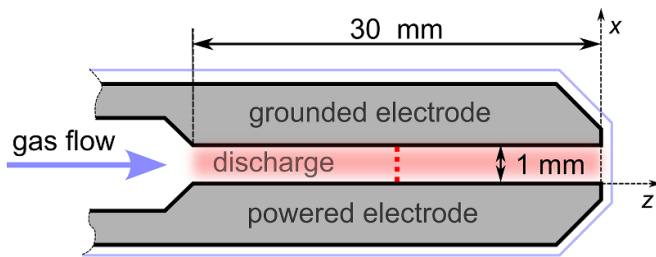
Figure 1. Schematic of the COST-jet head. The total volume of the discharge is 30 mm³. The vertical red dotted line shows the position (15 mm from the inlet) where experimental values were obtained.

density over plasma input power (figure 2(b)). The trend in the densities of all species considered follow that of the power: the highest absolute values are achieved in the 'peaks'/'valleys' case, due to the sharp voltage peak characteristic of these waveforms. However, this does not imply maximum efficiency in species generation with these waveforms, as the input power also peaks in these scenarios. This is indeed confirmed based on panels (c) and (d): in fact, as shown in panel (c), for O, the generation efficiency n_O/P is minimal for $\varphi = 0°$, 180°, and it exhibits a broader maximum near $\varphi = 90°$, 270°.

For He*, shown in panel (d), the generation efficiency follows the trend of the power, and the $\varphi = 0°$, 180° cases have the highest generation efficiencies. For $O_2(v)$, despite less dramatic efficiency variation, the 'peaks'/'valleys' waveforms yield local minima. Thus, while Voltage Waveform Tailoring effectively enhances the generation of radicals, the optimal waveform for achieving maximum energy efficiency depends on the specific species.

To elucidate the underlying reasons, figure 4 shows the cross sections of all relevant electron impact processes from

table 1 which are involved in generating the neutral species under investigation. Note, that it is sufficient to focus on electron impact processes (and not to discuss other chemical reactions), since, as demonstrated in, e.g. [16], the generation of these species is predominantly governed by the electron dynamics.

As shown in the figure, the cross sections corresponding to the generation of vibrationally excited oxygen (processes 7–10 in table 1) exhibit two 'branches', that is, there is a low energy region (between 0.2 and 2 eV) and a higher energy region (between 4 and 20 eV), where the cross sections are significant. For atomic oxygen, dissociative attachment (process 13, with a threshold of 4.2 eV) has the lowest threshold energy. However, at higher energies, dissociation (process 16, with a threshold of 8.4 eV) becomes the dominant process. The processes generating helium metastables, i.e. processes 2 and 3 have the highest threshold energies, around 20 eV.

Altering the voltage waveform (as per equation (1)) modifies the spatio-temporal electric field distribution, which affects the EEPF. Since the generations of the neutral species investigated here have distinct threshold energies, the electron impact source functions of O, $O_2(v)$, and He* will change differently as a function of φ, as demonstrated in figure 3. In order to explain this, we will investigate the $\varphi = 0°$ and 240° cases in more detail at which the most energy efficient generation of He* and O happens, respectively.

As seen in figure 5(a), which shows simulation results of the electric field distribution, E, for $\varphi = 0°$, the electric field exhibits a strong 'pulse' near $t/T = 0.5$, in accordance with figure 2(a). In this region, due to the rapid sheath collapse near the grounded electrode, the local Ohmic electric field is increased so that a sufficient number of electrons reaches the top electrode during the short local sheath collapse so that flux conservation of electrons and ions is maintained at this
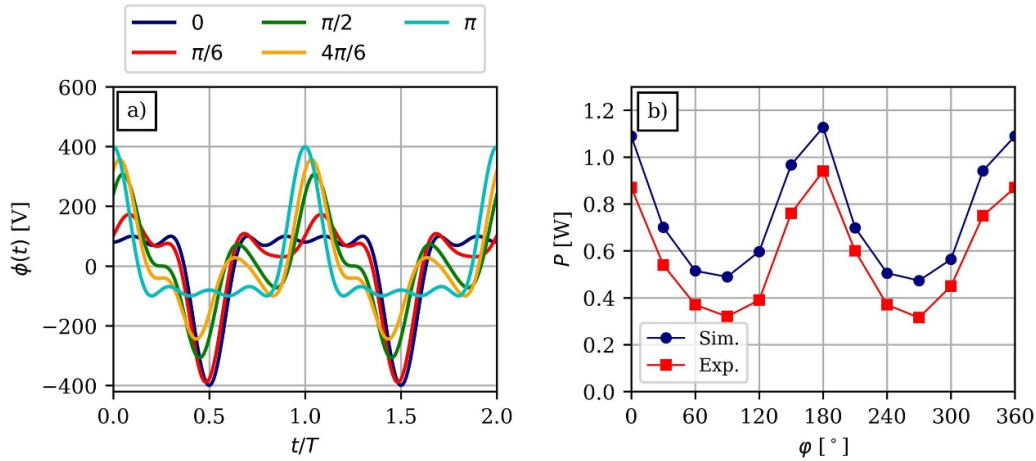
Figure 2. Excitation waveform, $\phi(t)$, for various phases, φ, over two RF-periods (a) and total input power, P, as a function of the phase from simulations and experiments (b). Discharge conditions: $p = 10^5$ Pa, $L = 1$ mm, $f_b = 13.56$ MHz, 99.5% He/0.5% O_2.
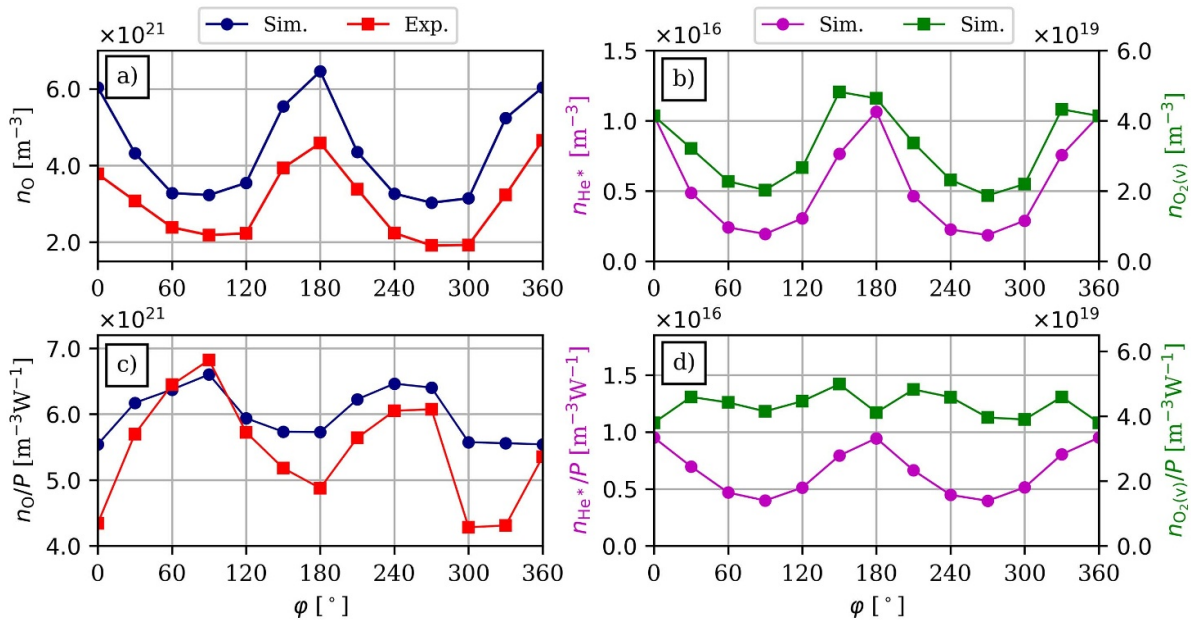

Figure 3. Spatially averaged atomic oxygen density, n_O, (a) and its generation efficiency, n_O/P (c) as a function of the phase, φ, obtained from simulation as well as experiments (TALIF), along with simulation data of the spatially averaged helium metastable density, n_{He^*}, and vibrationally excited oxygen density, $n_{O_2(v)}$, (b) as well as their generation efficiencies (d) as a function of phase.

electrode on time average [16]. Accordingly, in this spatio-temporal region, the electron impact source functions of the neutral species investigated here are elevated, which are shown in figures 5(b), (e) and (f) for He*, O and $O_2(v)$, respectively. For Helium metastable generation, peak rates occur where the electric field is strongest, notably during the local sheath collapse at the grounded electrode (indicated by the gray Region Of Interest (ROI)). This observation aligns with the experimental PROES findings (panel (c), showing excitation of the He I $(3s)^3S_1$ level from the ground state [32]), exhibiting excellent agreement with our simulation data. There is another region during sheath expansion near the powered electrode, represented by the green ROI, where S_{He^*} is non-negligible. This is in accordance with panel (d), which shows the EEPF, f_{EEPF} (normalized to the electron density), at distinct ROIs

indicated by the colored rectangles in panels (b), (e) and (f), as well as the mean EEPF (black line with star markers): in region III (corresponding to the energy interval where He* is primarily generated), the green and gray ROIs have the highest values; the other two EEPFs as well as the mean EEPF have a negligible contribution in this energy region.

Since the energy region for the generation of O has a lower threshold, the corresponding source function is considerable in regions where S_{He^*} is virtually negligible: this is shown in panel (e), where the EEPFs calculated in each of the ROIs have a significant contribution (region II, cf figure 5(e)). Panel (f) reveals that the electron impact source function of vibrationally excited O_2 peaks not only with the waveform's 'pulse' but also during subsequent 'ripples', particularly near $t/T \approx 0.8$. This occurs because, as shown in panel (d), the energy region
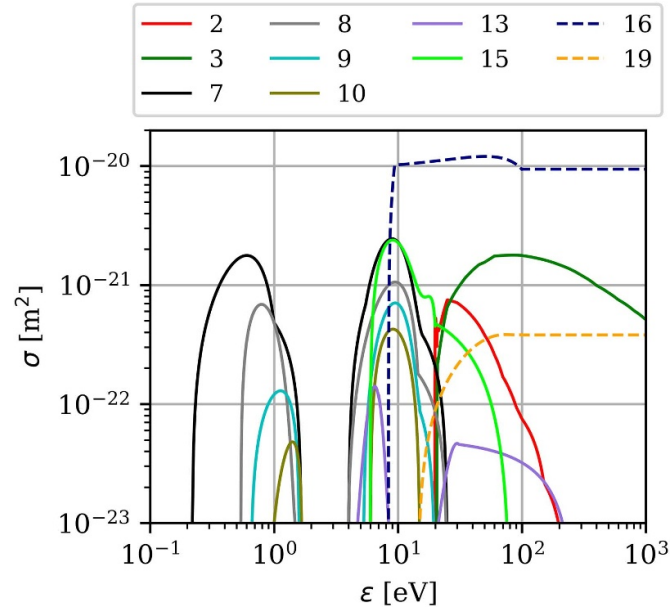
Figure 4. Cross sections of the electron impact processes, which involve the creation of either He*, O or $O_2(v)$, as a function of the electrons' Center-Of-Mass energy. The labels mark the processes listed in table 1.

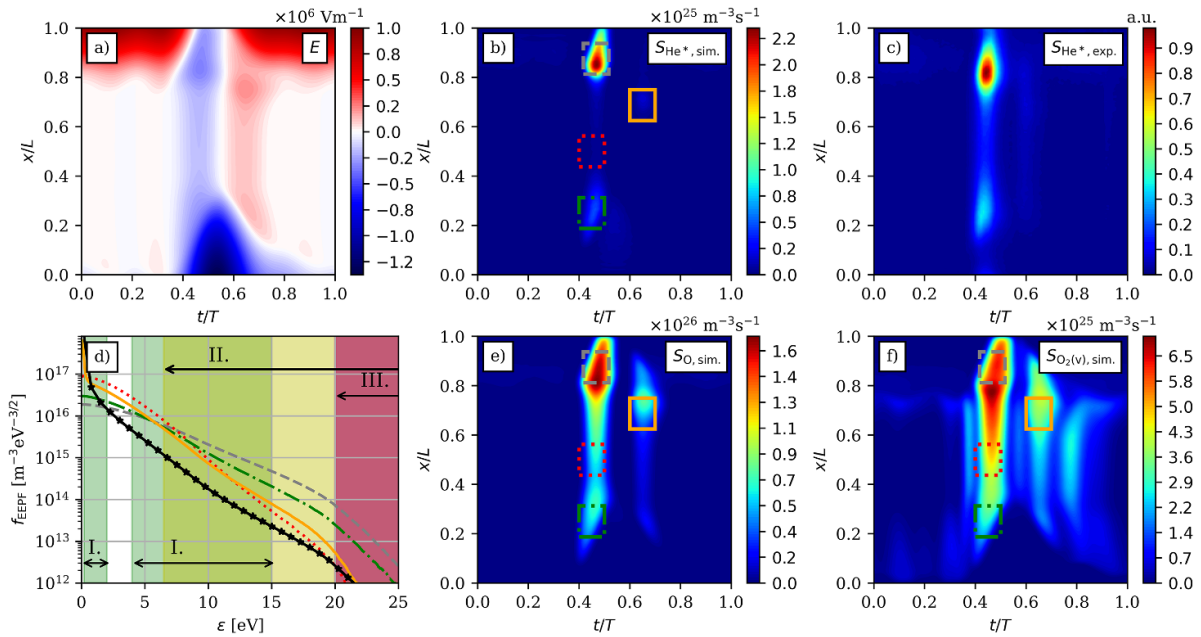**Figure 5.** Spatio-temporal distribution of the electric field, E (a), electron impact source function of He*, $S_{He*,sim.}$ (b), experimental (PROES) results for the excitation rate of the He I $(3s)^3S_1$ level from the ground state of He, $S_{He*,exp.}$ (c), electron energy probability functions, f_{EEPF} (d), electron impact source function of atomic oxygen, $S_{O,sim.}$ (e) and of the vibrational states of oxygen, $S_{O_2(v),sim.}$ (f) for $\varphi = 0°$. The lines in panel (d) are averages over spatio-temporal regions indicated by the colored rectangles in panels (b), (e) and (f). The black line with star markers in panel (d) represents the spatio-temporal average of the EEPF. I.-III. indicate energy regions where the cross sections of processes creating $O_2(v)$, O and He*, respectively, are considerable (cf figure 4).

where the generation of $O_2(v)$ is high, has a low energy branch: therefore, during the times of the main maximum and the smaller oscillations in voltage afterwards (cf figure 2) the energy of the electrons is sufficiently increased so that they can participate in generating vibrationally excited oxygen, unlike the other two neutral species considered. It is also worth noting, that based on panel (d), the higher energy branch is also important

in the generation of $O_2(v)$: the EEPF corresponding to the gray ROI, where $S_{O_2(v)}$ has the highest value, is depleted in the low energy part of region I.

The effect of 'ripples' is more clearly seen in figure 6, which shows the same physical quantities as figure 5, for $\varphi = 240°$. The crucial difference between the two cases presents itself in the electric field (a): while the 'valleys' (i.e. $\varphi = 0°$)
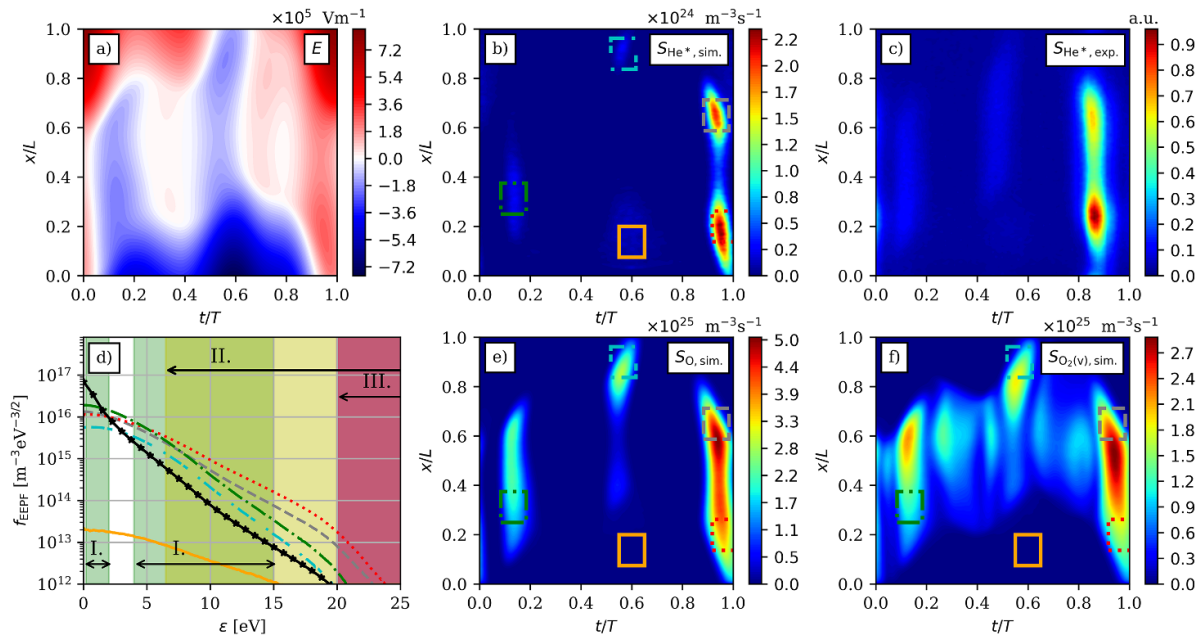
Figure 6. Spatio-temporal distribution of the electric field, E (a), electron impact source function of He*, $S_{\text{He*,sim.}}$ (b), experimental (PROES) results for the excitation rate of the He I $(3s)^3S_1$ level from the ground state of He, $S_{\text{He*,exp.}}$ (c), electron energy probability functions, f_{EEPF} (d), electron impact source function of atomic oxygen, $S_{\text{O,sim.}}$ (e) and of the vibrational states of oxygen, $S_{\text{O}_2(v),\text{sim.}}$ (f) for $\varphi = 240°$. The lines in panel (d) are averages over spatio-temporal regions indicated by the colored rectangles in panels (b), (e) and (f). The black line with star markers in panel (d) represents the spatio-temporal average of the EEPF. I.–III. indicate energy regions where the cross sections of processes creating $O_2(v)$, O and He*, respectively, are considerable (cf figure 4).

waveform, shows a single maximum (where the electric field is high and changes from positive to negative), the $\varphi = 240°$ scenario exhibits two distinct maxima at different times during one RF-cycle. Despite a lower maximum electric field, leading to the reduction of helium metastables (cf panels (b) and (c)), these local maxima deliver sufficient energy to electrons so that they generate atomic and vibrationally excited oxygen. As shown in panel (e), the electron impact source function of O is high in regions where the magnitude of the electric field is $\gtrsim 2 \times 10^5$ V m^{-1}. The electron impact source function of $O_2(v)$ (panel (f)) remains significant throughout the entire RF-cycle. This indicates that with this specific voltage waveform, the electron energy is 'spread' in time more evenly, leading to an efficient generation of vibrationally excited as well as atomic oxygen. These statements are in line with the EEPFs (d): although only the red and gray ROIs have EEPFs that have a non-negligible contribution in region III, i.e. helium metastable generation, all of them are significant in the other two energy regions. Taking this and the fact, that a smaller electric field magnitude leads to smaller input powers, we can arrive at the efficiencies presented in figure 3.

In summary, voltage waveform tailoring provides a way to control the generation of certain radical species. In this paper, we demonstrate how a specific one-parameter family of waveforms, comprising four consecutive harmonics and parameterized by the phase φ, enables control over the generation energy efficiencies of three highly relevant neutral species, i.e. helium metastable, atomic oxygen, and vibrationally excited oxygen. This control is achieved due to the dependence of the resulting EEPFs on the waveform and, consequently,

on the electric field distribution. Here, the generation energy efficiency is defined as the mean density of the given species divided by the input plasma power. Although, in absolute values, the 'peaks'/'valleys' waveform yields the highest numbers of these species due to the high electric field region during sheath collapse at the powered electrode, a different waveform demonstrated greater energy efficiency in generating neutral species with lower threshold energy, i.e. atomic and vibrationally excited oxygen. This efficiency results from the fact, that instead of one maximum of high electric field region, which favors the generation of He* due to its threshold energy of ≈ 20 eV, waveforms with multiple peaks with individually lower electric fields lead to (i) a lower input plasma power and (ii) electric fields too low for efficient helium metastable generation but high enough for the other two species, having significantly lower energy thresholds (0.19 eV for $O_2(v)$ and 4.2 eV for O) to be generated several times within a single RF-cycle.

While the presented results were generated for a specific gas mixture and with a focus on the generation of selected neutral species, similar results are expected under different discharge conditions for other neutral species as long as the electron energy thresholds of their generation vary and the EEPF is controlled by VWT.

Data availability statement

The data that support the findings of this study are openly available at the following URL/DOI: https://rdpcidat.rub.de/node/1052.

Acknowledgments

ORCID iDs

Máté Vass ⓘ https://orcid.org/0000-0001-9865-4982
David Schulenberg ⓘ https://orcid.org/0000-0002-4086-8678
Zoltán Donkó ⓘ https://orcid.org/0000-0003-1369-6150
Peter Hartmann ⓘ https://orcid.org/0000-0003-3572-1310
David Steuer ⓘ https://orcid.org/0000-0003-3005-0829
Marc Böke ⓘ https://orcid.org/0000-0003-1062-5808
Volker Schulz-von der Gathen ⓘ https://orcid.org/0000-0002-7182-3253
Ihor Korolov ⓘ https://orcid.org/0000-0003-2384-1243
Thomas Mussenbrock ⓘ https://orcid.org/0000-0001-6445-4990
Julian Schulze ⓘ https://orcid.org/0000-0001-7929-5734

References

[1] Adamovich I *et al* 2022 *J. Phys. D: Appl. Phys.* **55** 373001
[2] Von Woedtke T, Reuter S, Masur K and Weltmann K D 2013 *Phys. Rep.* **530** 291–320
[3] Graves D B 2014 *Plasma Proc. Polym.* **11** 1120–7
[4] Khlyustova A, Labay C, Machala Z, Ginebra M P and Canal C 2019 *Front. Chem. Sci. Eng.* **13** 238–52
[5] Dharini M, Jaspin S and Mahendran R 2023 *Food Chem.* **405** 134746
[6] Golda J *et al* 2016 *J. Phys. D: Appl. Phys.* **49** 084003
[7] Reuter S, Von Woedtke T and Weltmann K D 2018 *J. Phys. D: Appl. Phys.* **51** 233001
[8] Bruggeman P and Brandenburg R 2013 *J. Phys. D: Appl. Phys.* **46** 464001
[9] Steuer D, van Impel H, Gibson A R, Schulz-von der Gathen V, Böke M and Golda J 2022 *Plasma Sources Sci. Technol.* **31** 10LT01
[10] Korolov I, Steuer D, Bischoff L, Hübner G, Liu Y, Schulz-Von der Gathen V, Böke M, Mussenbrock T and Schulze J 2021 *J. Phys. D: Appl. Phys.* **54** 125203
[11] Jiang J and Bruggeman P J 2021 *J. Phys. D: Appl. Phys.* **54** 15LT01
[12] He Y *et al* 2021 *Plasma Sources Sci. Technol.* **30** 105017
[13] Sun B, Liu D, Iza F, Wang S, Yang A, Liu Z, Rong M and Wang X 2019 *Plasma Sources Sci. Technol.* **28** 035006
[14] Liu Y, Korolov I, Hemke T, Bischoff L, Hübner G, Schulze J and Mussenbrock T 2021 *J. Phys. D: Appl. Phys.* **54** 275204
[15] Mouchtouris S and Kokkoris G 2021 *Plasma Sources Sci. Technol.* **30** 01LT01
[16] Vass M, Schulenberg D, Donkó Z, Korolov I, Hartmann P, Schulze J and Mussenbrock T 2024 *Plasma Sources Sci. Technol.* **33** 015012
[17] Kushner M J 2009 *J. Phys. D: Appl. Phys.* **42** 194013
[18] Klich M, Wilczek S, Donkó Z and Brinkmann R P 2022 *Plasma Sources Sci. Technol.* **31** 045003
[19] Donkó Z 2022 *Plasma Sources Sci. Technol.* **31** 095006
[20] Vass M, Wilczek S, Schulze J and Donkó Z 2021 *Plasma Sources Sci. Technol.* **30** 105010
[21] Korolov I, Donkó Z, Hübner G, Liu Y, Mussenbrock T and Schulze J 2021 *Plasma Sources Sci. Technol.* **30** 095013
[22] Korolov I *et al* 2020 *J. Phys. D: Appl. Phys.* **53** 185201
[23] Derzsi A, Korolov I, Schüngel E, Donkó Z and Schulze J 2013 *Plasma Sources Sci. Technol.* **22** 065009
[24] Schmidt F, Schulze J, Johnson E, Booth J P, Keil D, French D M, Trieschmann J and Mussenbrock T 2018 *Plasma Sources Sci. Technol.* **27** 095012
[25] Wang J, Dine S, Booth J P and Johnson E V 2019 *J. Vac. Sci. Technol.* A **37** 021303
[26] Donkó Z, Hamaguchi S and Gans T 2018 *Plasma Sources Sci. Technol.* **27** 054001
[27] Liu Y, Korolov I, Trieschmann J, Steuer D, Schulz-von der Gathen V, Böke M, Bischoff L, Hübner G, Schulze J and Mussenbrock T 2021 *Plasma Sources Sci. Technol.* **30** 064001
[28] *Biagi-v8.9 Database (Cross Sections Extracted from PROGRAM MAGBOLTZ, VERSION 8.9 March 2010)* (available at: www.lxcat.net)
[29] Vahedi V and Surendra M 1995 *Comput. Phys. Commun.* **87** 179–98
[30] Gudmundsson J T, Kawamura E and Lieberman M A 2013 *Plasma Sources Sci. Technol.* **22** 035011
[31] Lafleur T 2015 *Plasma Sources Sci. Technol.* **25** 013001
[32] Schulenberg D A, Vass M, Klich M, Donkó Z, Klotz J, Bibinov N, Mussenbrock T and Schulze J 2024 *Plasma Chem. Plasma Proc.* **44** 1217–35